POLITECNICO DI TORINO
Repository ISTITUZIONALE

Structure-Property-Performance Relationships in a Low Band-Gap AgBiS2 Photoanodic Material

Original
Structure-Property-Performance Relationships in a Low Band-Gap AgBiS2 Photoanodic Material / Domenici, S., Ragonese, P., Marchini, E., Mazzanti, M., Landrot, G., Prato, M., Cara, E., Pozzati, M., Wittke, M., Wang, M., Caramori, S., Poli, I., Gatti, T.. - In: SMALL STRUCTURES. - ISSN 2688-4062. - 7:5(2026). [10.1002/sstr.70487]

Availability:
This version is available at: 11583/3011348 since: 2026-05-25T09:11:59Z

Publisher:
Wiley

Published
DOI:10.1002/sstr.70487

Terms of use:

This article is made available under terms and conditions as specified in the corresponding bibliographic description in the repository

Publisher copyright

(Article begins on next page)

26 November 2026

Small Structures

small structures

www.small-structures.com

RESEARCH ARTICLE OPEN ACCESS

Structure–Property–Performance Relationships in a Low Band-Gap $AgBiS_2$ Photoanodic Material

Sara Domenici[1,2] | Paola Ragonese[2] | Edoardo Marchini[3] | Michele Mazzanti[3] | Gautier Landrot[4] | Mirko Prato[5] | Eleonora Cara[6] | Micaela Pozzati[1] | Matthis Wittke[7] | Mengjiao Wang[1,2] | Stefano Caramori[3] | Isabella Poli[2] | Teresa Gatti[1,8]

[1]Department of Applied Science and Technology, Politecnico di Torino, Torino, Italy | [2]Center for Sustainable Future Technologies, Istituto Italiano di Tecnologia, Torino, Italy | [3]Department of Chemical and Pharmaceutical Sciences, University of Ferrara, Ferrara, Italy | [4]Synchrotron SOLEIL, L'Ormes des Merisiers, Saint Aubin, France | [5]Materials Characterization Facility, Istituto Italiano di Tecnologia, Genova, Italy | [6]Advanced Materials and Life Science Division, Istituto Nazionale di Ricerca Metrologica, Torino, Italy | [7]Institute of Physical Chemistry, Justus Liebig University, Giessen, Germany | [8]Center for Materials Research, Justus-Liebig University, Giessen, Germany

Correspondence: Isabella Poli (isabella.poli@iit.it) | Teresa Gatti (teresa.gatti@polito.it)

Received: 3 March 2026 | **Revised:** 13 April 2026 | **Accepted:** 13 May 2026

Keywords: annealing | perovskite-inspired material | photoanode | photoelectrocatalysis | silver bismuth sulfide

ABSTRACT

$AgBiS_2$ is a narrow-band-gap, water-stable semiconductor with strong visible-light absorption, making it a promising absorber material in devices for solar-driven photoelectrocatalysis. Despite extensive studies on its photovoltaic performance, the role of cation disorder in governing PEC activity remains unexplored. Here, we investigate this effect on solvothermally synthesized $AgBiS_2$ nanoparticles in photoanode thin films fabricated using ultrasonic spray coating. Mild thermal annealing partially homogenizes the cation distribution, as evidenced by lattice contraction in X-ray diffraction and absorption analyses, while spectroscopic characterization reveals subtle band-structure tuning toward a slightly n-type behavior. The annealed electrodes exhibit higher photocurrents and increased donor density. Impedance spectroscopy reveals improved hole flux to the semiconductor/electrolyte interface, while transient absorption spectroscopy identifies sub-bandgap trap-mediated recombination as the primary performance bottleneck. In addition, Operando X-ray absorption measurements show that annealing stabilizes the material under bias by suppressing ion migration. Together, these results reveal influences of thermal treatment on the structure and charge-carrier dynamics in $AgBiS_2$ photoanodes and support its implementation as low band gap material in electrode architectures. For the first time, we also demonstrate their optimal use with fast redox mediators for selective photooxidation and sustainable solar energy conversion.

1 | Introduction

Ongoing research on materials for photoelectrocatalysis (PEC) has focused on identifying candidates capable of driving a variety of solar-driven reactions, including water splitting, selective organic oxidation, CO_2 reduction, and several other redox processes. Wide bandgap semiconductors that can sustain photovoltages to drive unassisted water splitting are generally preferred as photoanodes, however, a main limitation lies in their limited light absorption mainly restricted to the ultraviolet region. Multijunction light absorbers are the best option to provide high photovoltages as well as photocurrents. For this reason, attention has shifted also toward materials with narrower band gaps, capable of harvesting a broader range of visible light, to be implemented in heterojunctions or tandem architectures with wide band gap materials [1]. Within this context, metal chalcogenides such as cadmium and lead sulfides/selenides have been extensively investigated owing to their strong light absorption and

This is an open access article under the terms of the Creative Commons Attribution License, which permits use, distribution and reproduction in any medium, provided the original work is properly cited.

© 2026 The Author(s). *Small Structures* published by Wiley-VCH GmbH.

favorable charge transport properties [2–4]. Similarly, lead halide perovskites (LHPs) have recently attracted significant interest due to their outstanding optoelectronic properties and exceptional light conversion efficiencies [5, 6]. Nonetheless, their practical use in PEC water splitting is hindered by toxicity concerns as well as their severe instability in aqueous media. As a response, research efforts have turned toward more sustainable alternatives that can provide similar advantages, reducing the associated issues [7]. Analogous materials based on heavy pnictogens, in particular those implementing bismuth, have gained increasing attention over the last decade, owing to their structural analogy to lead-based materials, their reduced toxicity, and their improved chemical stability in water. Inspired by the favorable attributes of conventional perovskites, bismuth-based double perovskites and perovskite-inspired materials have recently been under the spotlight for research on solar energy conversion [8, 9]. In particular, the incorporation of Bi^{3+} in crystal structures stabilized by monovalent cations has proven effective at mimicking the desirable properties of LHPs [10]. Among these structures, Ag-Bi materials exhibit several advantageous properties for wide-range optoelectronic applications [11], in particular Ag-Bi chalcogenides feature narrow band gaps, with strong optical absorption in the visible and near infrared range, making them highly effective for harvesting a broad portion of the solar spectrum. $AgBiS_2$ has already established its potential in solar cells, reaching efficiencies over 10% [12–16]. Additionally, it has shown exceptional resistance to moisture and maintaining structural integrity when immersed in water [17]. Owing to these advantages, this material has only recently been tested for the first time as a photoanode for water oxidation, showing promising performance under solar irradiation and good efficiency in the visible light range [18]. These early results strongly suggest that $AgBiS_2$ deserves further exploration as a candidate for PEC applications. Being a newly introduced material in this context, several factors require consideration to optimize its PEC performance, such as morphology, particle size, and surface chemistry. In particular, Park et al. have conducted a systematic study on the role of different ligands, demonstrating their substantial impact on PEC activity [18].

A peculiarity of these semiconductors is the tendency to crystallize with defects that go beyond conventional point vacancies and substitutional defects. Specifically, the deviation from an ordered crystalline arrangement of atomic positions in the cation sublattice, due also to similar ionic radii, is known as cation disorder [19]. It has been shown that this phenomenon significantly alters the optoelectronic properties of such semiconductors, opening up to attempts to optimize the desired properties through cation disorder engineering [20, 21]. A facile method to introduce homogenization of cation distribution is through thermal annealing. This method has shown increased performance in photovoltaic applications, owing to enhanced optical absorption and improved carrier transport [22, 23]. Mostly, this phenomenon was investigated on materials synthetized via hot injection [19, 22–24] and with $AgBiS_2$ thin films deposited either via spin-coating of nanoparticle inks [12, 23, 25–27] and molecular precursor solutions [28–30], or spray coating of molecular precursors [31]. Herein, we investigate for the first time the cation segregation and annealing-induced cation homogenization in solvothermally synthesized ligand-free $AgBiS_2$ nanoparticles, which are then processed into thin films by ultrasonic spray coating (USSC) [32–34]. We primarily study $AgBiS_2$ photoelectrodes using PEC water oxidation as benchmark reaction for extensive and robust photoanode characterization, and, for the first time, we introduce their potential as fast redox mediators for selective photooxidation.

2 | Results and Discussion

$AgBiS_2$ was synthesized via a facile solvothermal route inspired from an existing protocol reported in literature [35], using Ag^+ and Bi^{3+} nitrate salts, thiourea as sulfur source, ethylene glycol as solvent, and KBr and PVP as capping agents to control the geometrical shape of the nanoparticles during the crystal growth (details in Experimental Section). The mixture was poured in a Teflon-lined stainless-steel autoclave, and the reaction was carried out at 180°C for 40 min. The as-obtained black powder was analyzed via X-ray diffraction (XRD) to confirm the formation of ligand-free cubic phase (schapbachite) $AgBiS_2$ nanoparticles (Figure 1a). These nanoparticles show a rough octahedral shape with lateral sizes of around 60–80 nm, as shown from the TEM images in Figure S1a, b. Our approach extends thermal annealing as a cation disorder engineering strategy, typically applied to materials produced by alternative synthesis routes, such as hot-injection quantum dots. The thermal annealing in this case was performed at 250°C in a nitrogen-filled tubular oven. The XRD reflection positions exhibit slight shifts toward higher angles after thermal annealing, as shown in Figure 1b, suggesting a decrease in lattice constants, which aligns with several works reported in literature [20, 22, 23]. This contraction is attributed to the shortening of Ag—S bond lengths, associated with the transition from a cation-disordered to a relatively more homogeneous structure [23]. To gain a more in-depth evaluation of this phenomenon, extended X-ray absorption fine structure (EXAFS) spectra were analyzed, with a focus on Ag–S interatomic distance. The spectra for both samples are shown in Figure S2a, where the strong overlap between them indicates that the overall structure of the material remains largely preserved and has not been significantly disrupted by the annealing treatment. The magnitude of the fourier transform (FT) has the first peak at around 2 Å in the uncorrected FT spectra, considering a typical phase shift of roughly 0.5 Å. Thus, the actual absorber–scatterer, Ag–S, distance can be estimated to be around 2.5 Å for both samples. This value, however, is incompatible with a coordination sphere composed of six sulfur atoms as in the cubic structure (schapbachite), as expected by XRD results in Figure 1a, but rather suggests a lower S coordination number, more consistent with monoclinic acanthite (Figure S2c). Hence, similarly to what was already observed by Kesavan et al. [24], there is a contradiction between the XRD diffraction pattern, which reliably indicates the crystalline phase, and the EXAFS results. Fittings were carried out using the acanthite structural model (Figure S2c). The fitting results are reported in Table S1, and depicted in Figure 1d, e in the magnitude and real part of the FT space. The N parameter is consistent with acanthite structure, since Ag has two distinct sites coordinated by three and two sulfur atoms, respectively, giving an average of about 2.5 S atoms in the first coordination shell. In the work of Kesavan et al., the local structure was also found to be similar to acanthite phase from EXAFS fittings [24]. This discrepancy with the XRD pattern was explained using density functional theory and molecular

26884062, 2026, 5, Downloaded from https://onlinelibrary.wiley.com/doi/10.1002/sstr.70487 by Politecnico Di Torino Sist. Bibl Del Polit Di Torino, Wiley Online Library on [25/05/2026]. See the Terms and Conditions (https://onlinelibrary.wiley.com/terms-and-conditions) on Wiley Online Library for rules of use; OA articles are governed by the applicable Creative Commons License

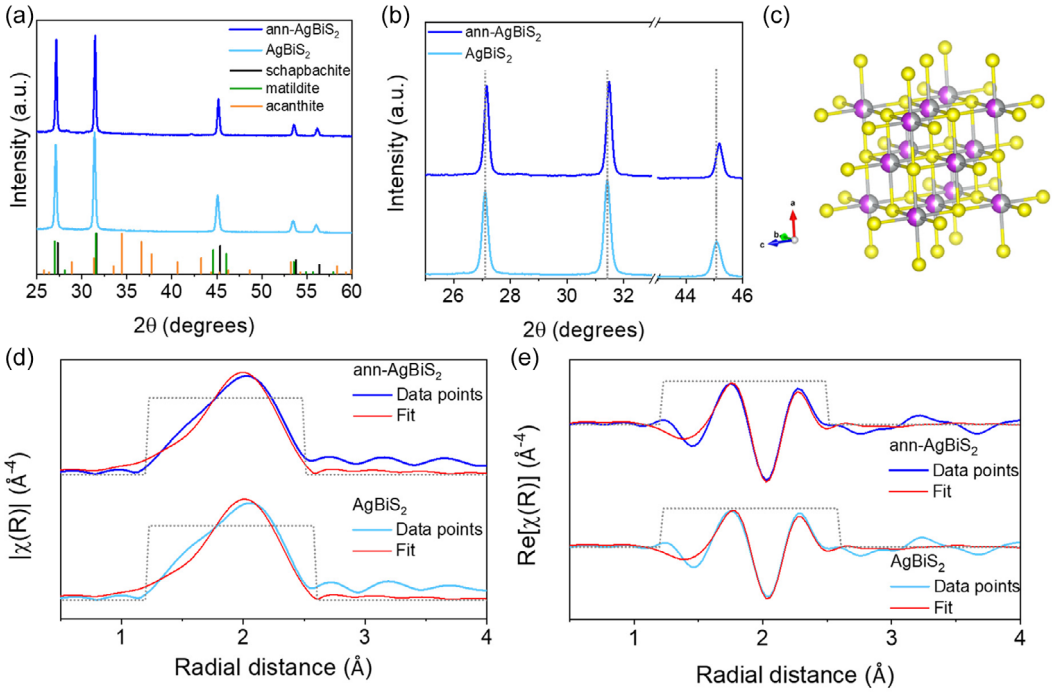

FIGURE 1 | Structural characterization of pristine and annealed $AgBiS_2$. (a) XRD patterns of the material before and after annealing and reference patterns of schapbachite (cubic), matildite (hexagonal) and acanthite (monoclinic) structures. (b) XRD inset highlighting the slight peak shifts for annealed $AgBiS_2$, (c) Cubic structure of $AgBiS_2$ showing homogeneous cation disorder. Ag K-edge EXAFS spectra in FT space, fittings in (d) magnitude and (e) real part. Fit details are provided in SI.

dynamics simulations. Their findings suggest that random Ag and Bi distribution on the cation sites of hexagonal matildite produces short Ag—S bonds due to local distortions, justifying the similarity to acanthite in the EXAFS spectra, while the overall lattice symmetry remains largely hexagonal. Homogeneous cation disorder in $AgBiS_2$, is defined as a random 50:50 distribution of Ag and Bi on cation sites, which has been shown to introduce intermediate electronic states between matildite and schapbachite in $AgBiS_2$ [22]. Thus, this material may be described as an intermediate structure maintaining long-range cubic lattice, whilst exhibiting local matildite-like arrangements with distorted interatomic distances [19]. Nonetheless, as reported in Table S1, a slight decrease of interatomic distances after thermal annealing was observed, consistent with the shifts in the XRD reflects, and the hypothesis of Ag—S bond shortening. Given the fitting uncertainties, the observed variation in interatomic distance provides an indication of the approximate lattice variation, rather than a quantitative measure of bond contraction.

The ultraviolet-visible-near infrared (UV–Vis–NIR) spectrum of nanoparticle inks in isopropanol was collected, showing a wide range of optical absorption, effectively covering the majority of the visible range, with a direct band gap extracted from the Tauc plot of 0.81 eV (Figure 2a). The optical absorption spectra of the nanoparticles reveal enhanced absorption in the NIR region after annealing, with a decrease in band gap to 0.75 eV (inset in Figure 2a). This narrowing in band gap is consistent with previous reports [19, 22]. Similar values are obtained using indirect band gap calculation (Figure S3), showing the same decrease from pristine to annealed sample. X-ray photoelectron spectroscopy (XPS) shows a slightly higher Bi atomic percentage relative to Ag and a slightly sub-stoichiometric S content for both pristine and annealed samples (Figure S4a,b,d,e, and Table S2), although the annealed material exhibits minor oxidation likely formed upon air exposure during this additional thermal step, restricting somehow the validity of stoichiometry considerations coming from surface analysis via XPS.

To further examine the electronic structure of solvothermal $AgBiS_2$, ultraviolet photoelectron spectroscopy (UPS) and XPS in the region of the valence band maximum (VBM) were employed to assess possible energy shifts following the thermal treatment. The results are summarized in Table S2. From the low-energy onset in the UPS spectra (Figure 2c) and the XPS spectra (Figure S4c, f), a slight increase in the VBM to Fermi level energy was observed, from 0.36 eV for the pristine sample to 0.40 eV after annealing. From the high energy onset in the UPS spectra, it was possible to calculate the work function (W_f) by subtracting the high energy onset value from the used photon energy (21.22 eV). The as-determined values for the pristine and the annealed samples are, respectively, 4.52 and 4.53 eV, suggesting that the thermal treatment does not affect the W_f. Based on these results, simplified band diagrams were constructed for both pristine and annealed materials, depicted in Figure 2b. It is clear from the scheme that pristine $AgBiS_2$ behaves as an intrinsic semiconductor, with the Fermi level located approximately in the middle of the band gap, in agreement with previous studies [29]. After annealing, the reduced band gap and slightly deeper VBM suggest a transition toward more enhanced n-type character, as also observed in literature [29]. Considering previous theoretical studies, a plausible explanation for the observed effects relies on the appearance of tail states in the conduction band, which lowers the conduction band minimum, also accounting for the narrowing of the band gap

26884062, 2026, 5, Downloaded from https://onlinelibrary.wiley.com/doi/10.1002/sstr.70487 by Politecnico Di Torino Sist. Bibl Del Polit Di Torino, Wiley Online Library on [25/05/2026]. See the Terms and Conditions (https://onlinelibrary.wiley.com/terms-and-conditions) on Wiley Online Library for rules of use; OA articles are governed by the applicable Creative Commons License

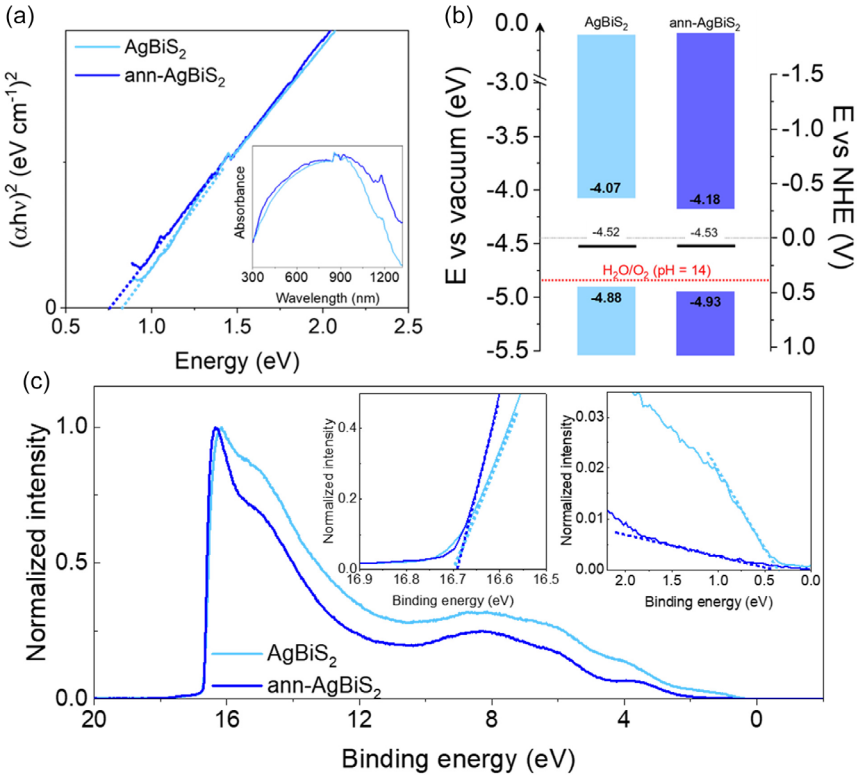

FIGURE 2 | Spectroscopic characterization of pristine and annealed $AgBiS_2$. (a) Tauc plots of the samples derived from absorption spectra, shown in inset. (b) Proposed band energy diagram constructed with the combined spectroscopic data. The black lines indicate the Fermi level positions. (c) UPS spectra with low- and high-energy onsets indicated in insets.

energy [19]. Moreover, the VB is localized on Ag-S states (interaction between Ag-4d and S-3p orbitals), whilst Bi–S states (interaction between Bi-6p and S-3p orbitals) dominate the CB [36]. A more homogeneous cation disorder promotes greater spatial delocalization of electronic states, enhancing charge-carrier mobility and transport properties [22]. The combination of these analyses suggests that cation disorder should also be evaluated when preparing this material using synthetic techniques other than hot injection.

Electrodes were prepared by USSC (see details in the Experimental Section) with varying number of deposition cycles, that is, 10, 20, 30, and 40 layers with annealed $AgBiS_2$. The film thickness and morphology were evaluated by cross-sectional scanning electron microscopy (SEM) (Figure 3a–c, Figure S5). The 10-layer sample exhibits a highly inhomogeneous profile with exposed regions of the back contact, and an overall thickness below 1 μm. Increasing the deposition to 20 layers resulted in complete coverage of the back contact, with thicknesses in the range of 1–1.5 μm. The 30-layer sample reached a thickness of ∼2 μm, whereas the 40-layer sample (Figure S5) achieved ∼3 μm but displayed significant cracking and inhomogeneities. The top-view of the pristine and annealed 30-layer samples (Figure 3d,e) suggest that the annealing treatment did not significantly impact the film morphology. Both films are highly porous, with homogeneously distributed particles smaller than 50 nm.

In order to gain insight into the electrochemical properties of the synthesized electrodes, dark cyclic voltammetry (CV) measurements of the $AgBiS_2$ in contact with 1 M KOH were performed (Figure S6a,b) by sweeping the voltage first toward the anodic (positive) direction and then reversing toward the cathodic region. The samples are hereon referred to as ABSX or ABSXann, where X indicates the number of deposited layers. ABS10, ABS20, and ABS30 revealed similar electrochemical features: the oxidation process appears irreversible, with the onset of the faradaic current found at ca. +0.18 V versus Ag/AgCl followed by a sharp peak at ca. +0.48 V versus Ag/AgCl which can be attributed to electron extraction from the density of states of the valence band, primarily composed by Ag and S orbitals. Upon scanning toward the cathodic branch, several minor waves are observed, but our attention is drawn by a broad and irreversible process occurring in the −0.47 V / −0.72 V versus Ag/AgCl range (also shown in Figure S6c). This can be ascribed to the population of trap states located in the sub-bandgap region, close to the conduction band edge. At more negative polarization, a further and more intense quasi-reversible wave appears, corresponding to the reduction of a higher density of electron-acceptor states, probably associated to the conduction band states composed of Bi orbitals. However, since the first explored oxidation process is irreversible, the cathodic region may be influenced by chemical changes occurred during the anodic scan. Therefore, the oxidation and reduction behavior was examined independently on fresh electrodes (Figure 4a). Under these conditions, the cathodic picture was slightly simplified, since it maintained the general features described above but lacked pre-waves at −0.02, −0.62 V versus Ag/AgCl and displayed a less pronounced shoulder at −0.72 V versus Ag/AgCl, indicating that, indeed, these electrochemical features are the consequence of irreversible changes to the electrode occurring during the anodic scan. Overall, despite the difficulty of dealing with chemically

26884062, 2026, 5, Downloaded from https://onlinelibrary.wiley.com/doi/10.1002/sstr.70487 by Politecnico Di Torino Sist. Bibl Del Polit Di Torino, Wiley Online Library on [25/05/2026]. See the Terms and Conditions (https://onlinelibrary.wiley.com/terms-and-conditions) on Wiley Online Library for rules of use; OA articles are governed by the applicable Creative Commons License

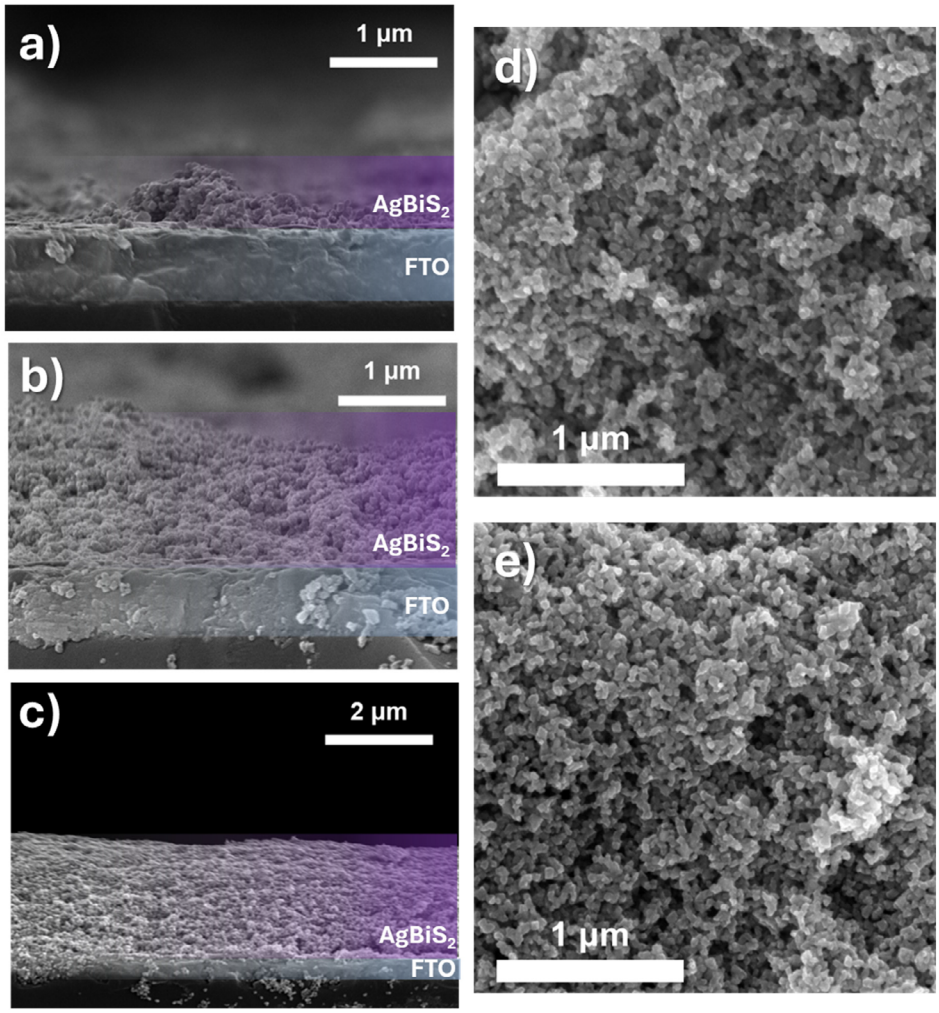

FIGURE 3 | Cross-section SEM of the electrodes with different thicknesses preparedvia USSC, (a) 10, (b) 20, and (c) 30 layers. Top-view SEM images of 30 layers sample (d) pristine and (e) postannealing.

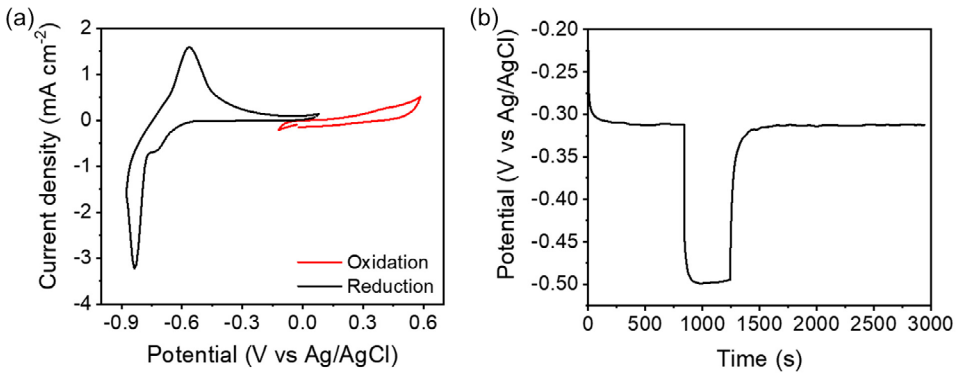

FIGURE 4 | Electrochemical characterization of a representative $AgBiS_2$ 20-layer based electrode. (a) CV in contact with 1 M KOH solution and (b) open-circuit potentiometry under simulated sunlight in contact with 0.5 M sodium ascorbate. Potentials are reported versus Ag/AgCl since protons are not potential determining ions for $AgBiS_2$.

irreversible processes, the electrochemical gap that we can extract from the onsets of the voltammetric waves appears to be essentially consistent with the optical gap of ~0.8 eV.

We gained confirmation of the electrochemical levels by estimating the flat band potential (E_{FB}) of the $AgBiS_2$ through photovoltage relaxation in the presence of a fast hole scavenger, sodium ascorbate, shown in Figure 4b. The open circuit photovoltage afforded a value of ca. −0.49 V versus Ag/AgCl (0.16 V vs. RHE), in good agreement with the onset of the reductive process occurring at ca. −0.52 V versus Ag/AgCl in Figure 4a. By using this value as an approximate indication of the conduction band edge and the optical bandgap, we find a valence

26884062, 2026, 5, Downloaded from https://onlinelibrary.wiley.com/doi/10.1002/sstr.70487 by Politecnico Di Torino Sist. Bibl Del Polit Di Torino, Wiley Online Library on [25/05/2026]. See the Terms and Conditions (https://onlinelibrary.wiley.com/terms-and-conditions) on Wiley Online Library for rules of use; OA articles are governed by the applicable Creative Commons License

band edge at ca. +0.31 V versus Ag/AgCl, in good agreement with the onset of the anodic process in Figure 4a,b, corroborating thus the indication that the main electrochemical features we observe with these electrodes are indeed originated by the frontier density of states of the semiconductor.

To obtain more information on photogenerated carrier properties, a combination of different electrochemical characterizations was necessary. PEC response in aqueous KOH was investigated, with the aim of using water oxidation as a benchmark reaction to thoroughly characterize the properties of $AgBiS_2$ as photoanode material and to reliably understand carrier dynamics.

The PEC performance of samples before and after annealing and with varying thicknesses were compared. The corresponding LSV curves are presented in Figure 5a–d. The onset potential remains unchanged with varying film thickness, and for all samples, the photocurrent at 0.9 V versus RHE (unbiased condition) is comparable to that at 1.23 V versus RHE. A stable and illumination-independent feature at 1.2 V may suggest surface passivation, in both annealed and pristine samples. An increase in photocurrent was observed with increasing deposition cycles, reaching a maximum at 30 layers, whereas a significant quenching of photocurrent occurred for the 40-layer sample. In this case, the ~3 µm thick film greatly exceeds the effective carrier diffusion length, leading to enhanced bulk recombination losses, limiting light penetration and hindering efficient charge transport from the surface to the back contact. Moreover, poor film quality (shown in Figure S5) can further disrupt charge transport pathways and contribute to performance losses. Nonetheless, in all cases, thermal treatment led to a marked increase in photocurrent with respect to the pristine samples as an effect annealing-induced

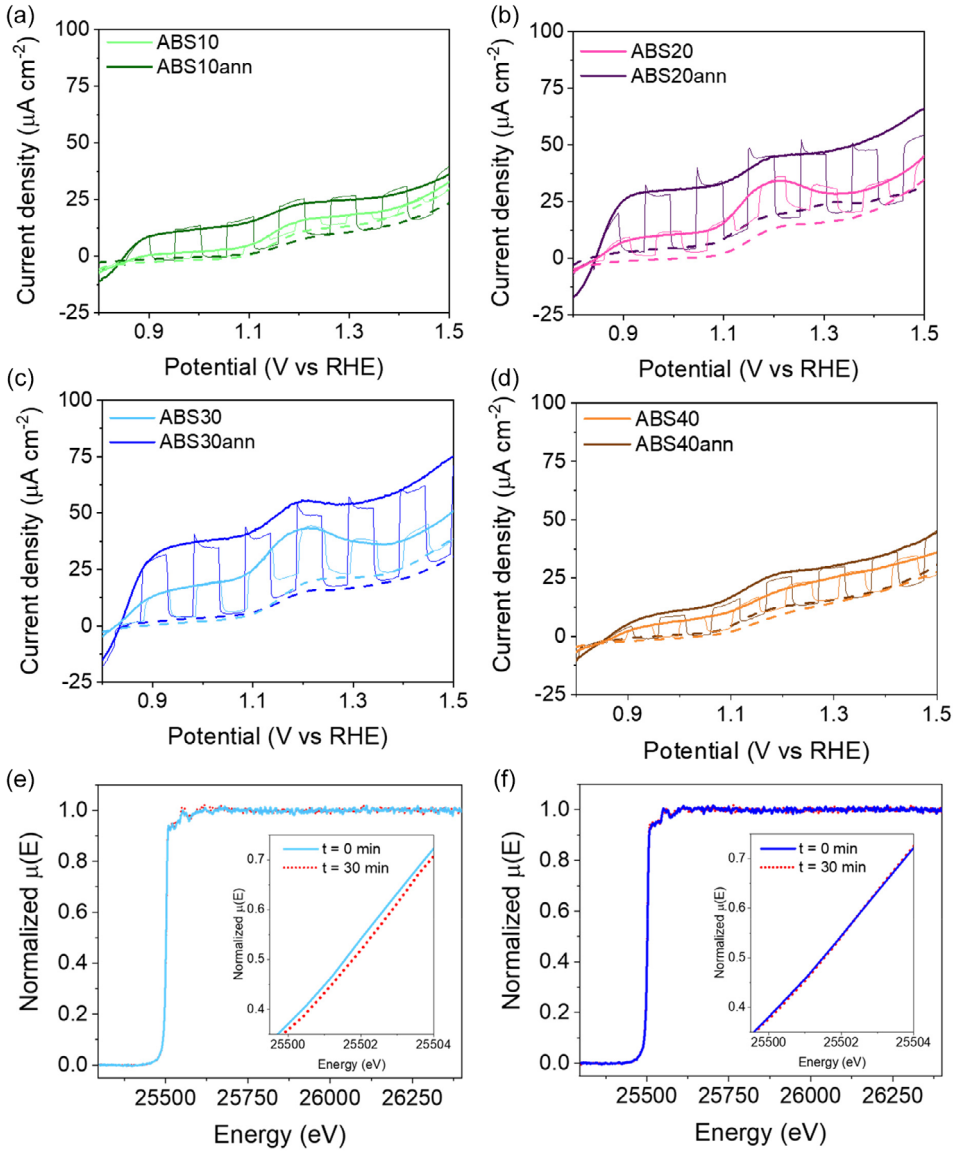

FIGURE 5 | PEC characterization of the different $AgBiS_2$ thin film photoanodes with pristine and annealed material. Linear sweep voltammetry (LSV) curves showing dark currents (dashed lines), light currents (thick solid lines) and chopped LSV curves (solid thin lines) of electrodes with (a) 10, (b) 20, (c) 30, and (d) 40 layers. Further characterizations on ABS30 and ABS30ann. Operando X-ray absorption spectroscopy (XAS) during a 30 min long chronoamperometry at 1.23 V versus RHE in dark with insets showing the X-ray absorption near edge structure (XANES) region of (e) pristine and (f) annealed $AgBiS_2$.

26884062, 2026, 5, Downloaded from https://onlinelibrary.wiley.com/doi/10.1002/sstr.70487 by Politecnico Di Torino Sist. Bibl Del Polit Di Torino, Wiley Online Library on [25/05/2026]. See the Terms and Conditions (https://onlinelibrary.wiley.com/terms-and-conditions) on Wiley Online Library for rules of use; OA articles are governed by the applicable Creative Commons License

band energy modulation. To investigate the direct correlation between the thermal treatment and increased PEC performance more in depth, we focused on the samples with 30 layers, ABS30 and ABS30ann, which reached the highest photocurrent, hence indicating that 30 layers deposition achieves most effective catalyst loading. Mott–Schottky analysis was used to estimate changes in the donor density concentration with the annealing treatment (Figure S7). The positive slope confirms the slightly n-type behavior. The donor density concentration of the electrode material was calculated through the Mott–Schottky equation (see Experimental Section for details), and increases from 1.4×10^{19} cm^{-3} for the pristine sample to 2.0×10^{19} cm^{-3} for the annealed one, consistent with an enhanced PEC activity. The flat band potential (E_{FB}) of the two samples was also determined to be 0.17 V versus RHE for the pristine sample and 0.19 V versus RHE for the annealed one, consistent with the results reported in Figure 4b (0.16 V vs. RHE), but indicating no particular change induced by the treatment. At 1.23 V versus RHE, the relative chronoamperometry curves were measured (Figure S8a–d), showing anodic transients for the annealed samples, which may indicate a larger population of photogenerated holes becoming temporarily accumulated at surface or sub-surface states before being extracted, delaying recombination dynamics [37]. Incident photon-to-current conversion efficiency (IPCE) was also measured at 1.23 V versus RHE, shown in Figure S9a–c. Although the photocurrent and efficiency of these photoanodes are quite low, understanding the effect of annealing in PEC applications offers meaningful information for future optimizations and for the investigation of other PEC reactions.

Operando XAS was performed to further investigate possible partial changes in oxidation states of the elemental components of $AgBiS_2$. A chronoamperometry measurement was carried out in dark at 1.23 V versus RHE for 30 min, and the XAS measurements were carried out at the Ag K-edge (Figure 5e,f). Particularly, by observing the XANES region of the spectra at the beginning and at the end of the chronoamperometry, a slight shift to lower energy is present, indicating a minor apparent change of the partial oxidation state of silver, as shown in the zoomed-in insets in Figure 5e. In the annealed sample, however, the two curves at the beginning and at the end of the chronoamperometry overlap (inset in Figure 5f). The minor increase in oxidation state could be associated with local geometric changes [38, 39], linked to ion movement occurring with the aid of an electric bias [40, 41]. As this is not observed for the annealed sample, this suggests that the annealing treatment helps to suppress such process. Previous reports have shown that cation disorder induces local charge imbalances that stabilize sulfur vacancies, working as deep trap states and limiting seminconductor performance [11]. A reasonable interpretation is that, in the pristine material, the S vacancies provide sites that facilitate ion migration under bias, which may manifest as the observed XANES shift. On the contrary, annealing likely decreases the vacant site density, suppressing the bias-induced ion redistribution, and hence stabilizing the Ag oxidation state. Further in-depth investigations are necessary to fully elucidate this phenomenon and will be subject of future work.

To further investigate the evolution of charge transport, charge transfer and recombination processes upon annealing, small perturbation techniques such as photoelectrochemical impedance spectroscopy (PEIS) and Intensity-modulated photocurrent spectroscopy (IMPS) were used. Figure 6a,b shows the Nyquist plots of ABS30 samples, measured under dark and simulated one sun illumination in 1 M KOH at 0.9 V versus RHE. The impedance semicircles of both samples decrease significantly under illumination. Upon light exposure, electron–hole pairs are generated and transferred to the photoelectrode/electrolyte interface to drive the OER, thereby lowering the overall internal resistance compared to the dark condition. The Nyquist plots of both ABS30 and ABS30ann were fitted using the same two-RCPE (resistor in parallel with constant phase element) in series as unit equivalent circuit, with a high frequency (HF) and a low frequency (LF) component. This equivalent circuit includes three resistances: a series resistance (R_S) attributed to the contact electrode, a bulk transfer resistance (R_t) associated with fast processes within the film and at the substrate/photoanode interface (HF semicircle), and a surface resistance (R_{surf}) associated with slower interfacial processes occurring at the semiconductor/liquid junction (LF semicircle). For both samples, R_{surf} is significantly larger than R_t, indicating that surface-related processes dominate the impedance response (see Table S4 for details). R_{surf} of ABS30ann is approximately three times smaller than in the not-annealed ABS30, suggesting that the annealing enables easier charge transfer at the photoelectrode/electrolyte interface. This improvement can be attributed to annealing-induced changes in the electronic structure, which reduce energetic barriers at the photoelectrode/electrolyte interface and facilitate hole extraction. This trend is consistent with the photocurrent densities shown in Figure 5. To isolate the contribution of bulk processes, PEIS was repeated using a hole scavenger electrolyte. Different hole scavengers were tested (Figure S10), and sodium ascorbate 0.5 M was found to be an effective hole scavenger for this photoanode material (Figure S11). Under these conditions, the Nyquist plots of both samples can be fitted using a single RC-unit equivalent circuit, corresponding to the bulk transfer resistance (Figure 6b,c). The two samples show similar semicircles, consistent with the comparable dJ/dV at 0.5 V versus RHE measured for ABS30 and ABS30ann (see Fig S11c, Table S5). IMPS measurements were performed to complement PEIS outcomes and provide further insight into the dynamics of photogenerated carriers. Unlike PEIS, which modulates the applied voltage, IMPS applies small perturbations to the light intensity at a fixed potential and probes the resulting photocurrent response. Figure S12 shows the IMPS spectra for ABS30 before and after annealing, recorded in the scavenger electrolyte at 0.5 V versus RHE. Both spectra exhibit a single semicircle located in the fourth quadrant. The intercept of the semicircle on the real axis represents the modulated photocurrent and reflects the hole flux arriving at the surface. The annealed sample displays a substantially larger semicircle than the pristine ABS30 without annealing, indicating a larger hole flux at 0.5 V versus RHE, consistent with the photocurrent results and with the reduced R_{surf} observed in PEIS, improved charge transport to the surface and efficiency of interfacial hole transfer. None of the samples exhibit a semicircle in the first quadrant, confirming negligible surface recombination, as expected when using a hole scavenger electrolyte. The annealing step enables both higher hole flux arriving at the surface and easier charge transfer at the photoelectrode/electrolyte interface.

Further mechanistic studies were carried out though spectroelectrochemistry and transient absorption spectroscopy (TAS) on thinner films (due to excess absorption of thicker ones for optical

26884062, 2026, 5, Downloaded from https://onlinelibrary.wiley.com/doi/10.1002/sstr.70487 by Politecnico Di Torino Sist. Bibl Del Polit Di Torino, Wiley Online Library on [25/05/2026]. See the Terms and Conditions (https://onlinelibrary.wiley.com/terms-and-conditions) on Wiley Online Library for rules of use; OA articles are governed by the applicable Creative Commons License

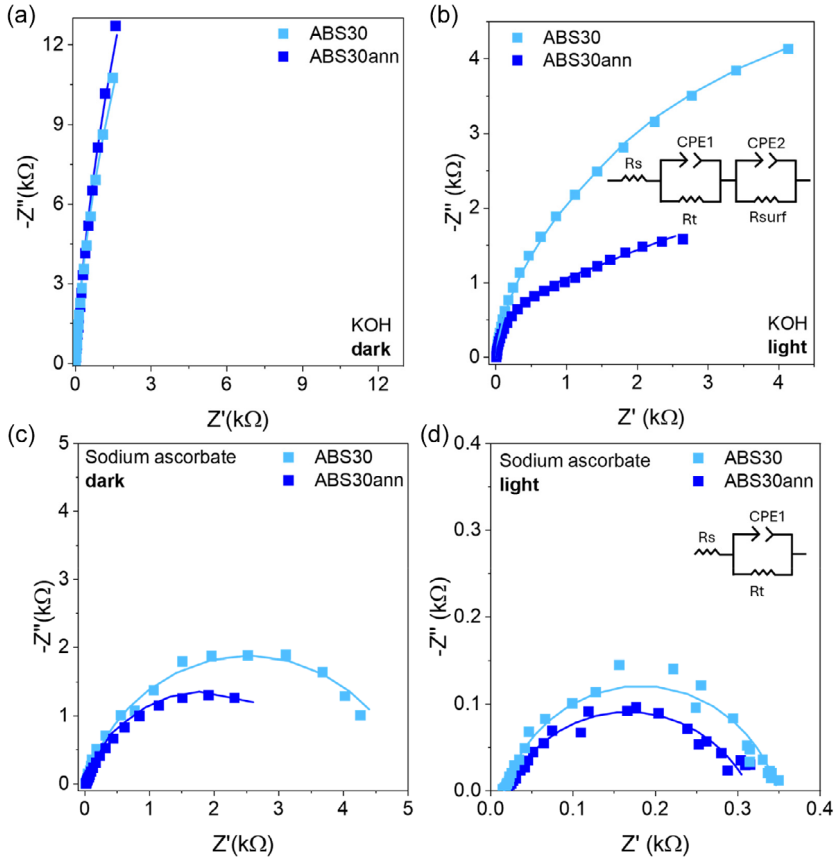

FIGURE 6 | PEIS at 0.9 V versus RHE in 1 M KOH a) under dark and b) simulated 1 sun illumination. EIS at 0.5 V versus RHE in 0.5 M sodium ascorbate c) under dark and d) simulated 1 sun illumination. Points are measured data while continuous lines are the Z-fit (see SI for details).

measurements in transmission mode), in order to fully unravel potential and limitations of $AgBiS_2$ as photoanode material. Spectroelectrochemistry of ABS20ann in contact with 1 M KOH did not reveal meaningful ΔA changes under anodic conditions, whereas a detectable and partially reversible change in the optical absorption of the electrode was detected under cathodic polarization, corresponding to the filling of electron acceptor states both in the proximity and within the conduction band. Despite the semi-opaque nature of the electrode, which caused a relatively low signal-to-noise (S/N) ratio of the difference spectrum, a positive ΔA signal extending in the visible and NIR region, starting from a maximum at 480–500 nm and assigned to electron absorption, was revealed (Figure S13).

TAS was first carried out in transmission mode on more transparent, ABS10ann samples, in the presence of a fast hole scavenger (0.5 M sodium ascorbate), in order to extract information about the photoexcited electron dynamics. Consistent with the SEC analysis, the TA spectrum recorded in the visible region under open circuit conditions (disconnected wires) displayed a positive profile with a well-defined band centered around 480 nm, followed by a flat, featureless absorption extending from 500 to 800 nm (Figure 7a). Within the instrumental sensitivity the ground state recovery appears to be completed within 4 μs. We investigated the potential dependent kinetics at 480 nm, in correspondence of the relatively well-defined absorption band that was observed in steady state spectroelectrochemistry as well. We observed that the initial amplitude at 480 nm progressively increased under positive bias, from 9 to 12 mΔOD, consistent with a partial suppression of fast recombination events, whose kinetics are outside of the IRF of our spectrometer, but that still affect the initial population of photoexcited electrons (Figure 7b). The increase in the initial ΔA amplitude is attributed to the electric field applied through the potentiostat which spatially separates electrons and holes within the $AgBiS_2$ substrate, slowing down their recombination. However, the ΔA versus V plot (Figure S14) shows only a modest correlation with the normalized JV characteristic measured under identical conditions. Only a slight increase of ΔA is indeed observed when moving from open circuit conditions to the photocurrent plateau region. This suggests that, while the effect of the bias on the transient kinetics reflects to some extent the photocurrent generation mechanism, most of the transient amplitude we are observing is unable to contribute to the photocurrent, recombining inside the electrode well before being revealed by the electrometer. This is again consistent with the maximum IPCEs of ca. 2% recorded with the best electrodes with ascorbic acid, which indicates that ca. 98% of the carriers are lost through recombination (Figure S11). The effect of the bias on the charge carriers is evident also through the decay kinetics. Here a multiexponential function was used to calculate an amplitude-weighted lifetime accounting for a distribution of recombination events with different rate constants, arising from the intrinsically heterogeneous nature of the mesoporous substrate (Figure S15). A general voltage dependence of the average lifetime was observed upon applying positive bias: initially, the lifetime increases, indicating that recombination slows down with increasing electron–hole spatial separation (Table S6). A maximum $<\tau>$ of ca. 410 ns was achieved around 0.445 V versus RHE, which corresponds to the region of the highest film

26884062, 2026, 5, Downloaded from https://onlinelibrary.wiley.com/doi/10.1002/sstr.70487 by Politecnico Di Torino Sist. Bibl Del Polit Di Torino, Wiley Online Library on [25/05/2026]. See the Terms and Conditions (https://onlinelibrary.wiley.com/terms-and-conditions) on Wiley Online Library for rules of use; OA articles are governed by the applicable Creative Commons License

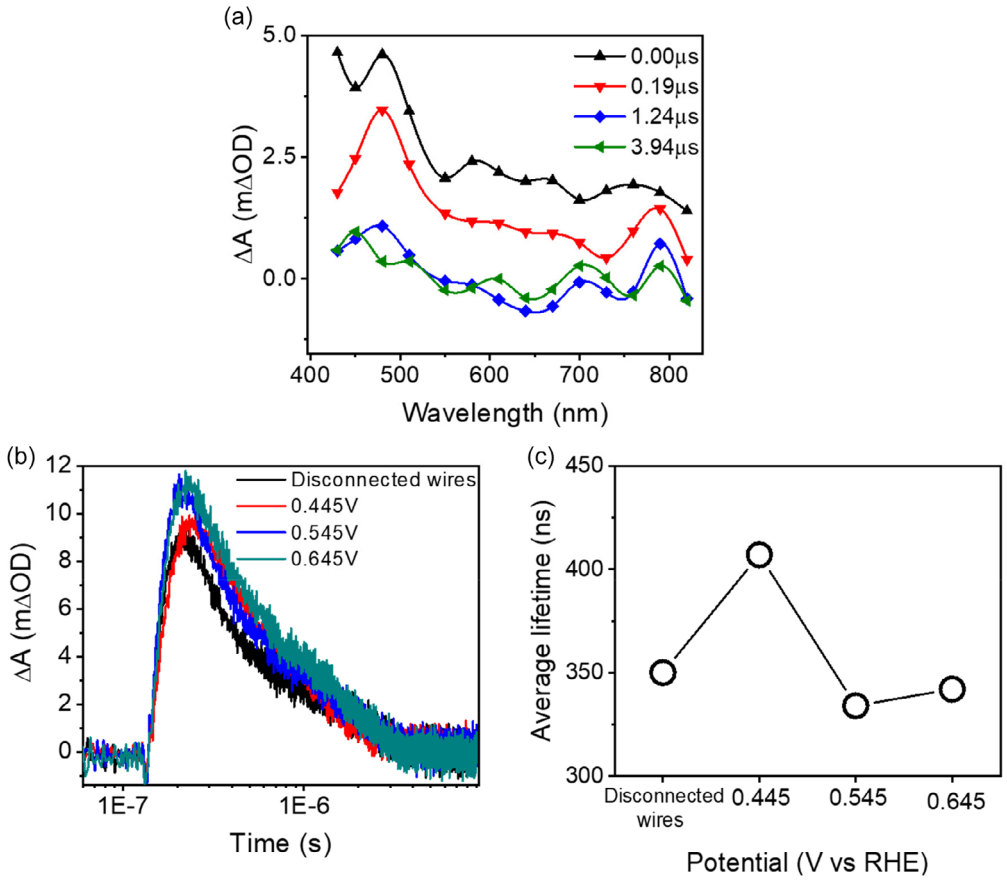

FIGURE 7 | (a) Transient absorption spectrum and (b) decay kinetics at 480 nm measured at variable applied potentials for ABS10ann in contact with 0.5 M ascorbate solution. (c) Average lifetime of the 480 nm traces as a function of the applied voltage computed from multiexponential fitting of the kinetics data reported in (b).

conductivity (Figure S16). At higher positive potentials the lifetime decreases, due to concurrent electron extraction from the material and the sweeping of the holes toward the electrode/electrolyte interface, where they are partially consumed by ascorbate [42]. In the absence of the fast sacrificial agent, that is, in the presence of KOH, the TA spectra exhibited similar features: an e^--associated fingerprint followed by the flat, featureless absorption (Figure S17). However, here, the higher activation barrier and lower driving force for more demanding H_2O and OH^- oxidation results in 99.9% recombination of the photogenerated carriers (0.1% of IPCE) and no meaningful potential dependence of the initial ΔA amplitude and lifetime was observed. Nevertheless, we could confirm that in the absence of a fast hole scavenger, a significantly shorter lifetime of 180 ns was obtained, much shorter than the expected time frame for interfacial charge transfer in complex multi electron transfer reactions, like the OER, usually occurring in the ms/s time scale, explaining the very low quantum yields of this new material when employed in such conditions (Figure S18). Similar conclusions can be drawn from the study of ABS20ann electrodes whose opacity, however, makes transmission transient spectroscopy more problematic for a good S/N of the oscillographic traces. Also in this case we found a longer electron lifetime when the semiconductor scaffold was in contact with 0.5 M ascorbate solution rather than KOH (Figure S19), corroborating the 10-fold higher photocurrent achieved in the presence of fast hole scavengers.

Finally, operational stability tests were conducted. Particularly, the binder-free, spray-coated nanoparticle films exhibit a loose

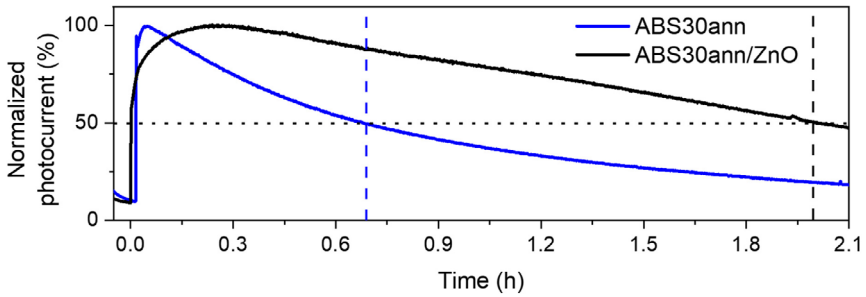

FIGURE 8 | Operational long-term PEC stability test at 1.23 V versus RHE under light exposure of ABS30ann with and without the ALD deposited ZnO protective layer.

26884062, 2026, 5, Downloaded from https://onlinelibrary.wiley.com/doi/10.1002/sstr.70487 by Politecnico Di Torino Sist. Bibl Del Polit Di Torino, Wiley Online Library on [25/05/2026]. See the Terms and Conditions (https://onlinelibrary.wiley.com/terms-and-conditions) on Wiley Online Library for rules of use; OA articles are governed by the applicable Creative Commons License

structure, as seen in the SEM images in Figure 3d,e, making film delamination a potential concern. Hence, a longer chronoamperometry at 1.23 V versus RHE was recorded to monitor photocurrent decay over time (Figure 8). For ABS30ann, the photocurrent was halfed after roughly 45 min, and approached a value close to the dark current contribution after 2 h. To enhance the stability of the phtoanodes by hindering the delamination of the film, a thin layer (estimated thickness of ∼17 nm) of ZnO was deposited via atomic layer deposition (ALD) on top of the $AgBiS_2$ surface (see details in the Experimental Section). The presence of the ALD-deposited layer does not result in either enhanced, nor hindered PEC performance, as shown from the LSV curve in Figure S20, proving that such layer has only a protective function toward material delamination during operation. Similar approaches have been already used in the literature and demonstrated significantly improved operational stability [43, 44]. Indeed, the protected electrode here shows a substantially slower decay, reaching 50% of the maximum photocurrent after a little over 2 h.

3 | Conclusions

In summary, this study presents $AgBiS_2$ photoelectrodes prepared with solvothermally synthesized nanoparticles and the USSC deposition technique. We have observed that cation disorder is relevant even for particles obtained through this synthetic route, and that a facile annealing step provides a straightforward means to modulate these local structural characteristics, as supported by XRD and XAS, and band energy changes, observed spectroscopically. The spray-coated electrodes were tested for PEC OER both to test the suitability of $AgBiS_2$ as a photoanode for solar water splitting and to provide a reliable benchmark oxidation reaction. We observed that the annealed photoelectrode shows enhanced performance compared to the pristine ones. Moreover, Operando XAS reveals that only pristine samples show bias-induced slight changes in Ag oxidation state, hinting that annealing treatment may reduce vacant site density, and hence vacancy-assisted ion migration. With the aid of a hole scavenger, IMPS and PEIS show that annealing increases the flux of photogenerated holes that reach the surface and facilitates the charge transfer across the interface. Nonetheless, TAS confirms that, even in the scavenger solution, most carriers recombine before contributing to photocurrent, explaining the low IPCE values and recognizing recombination as the performance bottleneck in this electrode architecture. The behavior of simple $AgBiS_2$ photoanodes suggest that future investigations should be conducted on its implementation of as low band gap material in tandem or heterojunction architectures with wide band gap semiconductors. Moreover, the here thoroughly elucidated dynamics in the $AgBiS_2$ electrodes suggest that the best use of this material in PEC applications should be in association with fast redox couples where this material can capitalize on its exceptional light harvesting and mild potential to drive selective oxidation reactions, for example in the growing field of biomass valorization.

4 | Experimental Section

4.1 | Materials

Bismuth(III) nitrate pentahydrate ($Bi(NO_3)_3{\cdot}5H_2O$), silver nitrate ($AgNO_3$), thiourea, potassium bromide (KBr) and polyvinyl pyrrolidone (PVP, MW 29K) and ethylene glycol were purchased from Sigma–Aldrich. Fluorine-doped tin oxide (FTO) coated glass substrates were purchased from Sigma–Aldrich.

4.2 | Synthesis of $AgBiS_2$ Nanoparticles

The nanoparticles were prepared via solvothermal synthesis, modified from an existing protocol [35]. 0.176 mmol of $AgNO_3$, 0.176 mmol of $Bi(NO_3)_3{\cdot}5\,H_2O$ and 200 mg of PVP were dissolved in 10 mL of ethylene glycol. 0.460 mmol of thiourea were dissolved in 10 mL of ethylene glycol, and 1.00 mmol of KBr was dissolved in 5 mL of ethylene glycol. The three mixtures were left stirring at room temperature for roughly 1 h. Once all the compounds were fully dissolved, the mixtures were poured together in the same beaker and stirred. The final mixture was transferred to a 50 mL Teflon-lined autoclave and placed in an oven at 180°C for 1 h. The product was collected via centrifugation by washing with deionized water and ethanol (3 times each). Annealing of the powders was performed in a N_2 filled tube furnace at 250°C for 1 h, with a heating ramp of 2.5°C min^{-1}. This annealing temperature was selected based on preliminary Mott–Schottky characterization (Figure S21) of samples annealed at 200 or 250°C, choosing the 250°C as it exhibits higher carrier density, in order to reliably investigate the correlation between annealing and charge carrier properties.

4.3 | Materials Characterization

The UV–vis-NIR diffuse reflectance spectra were recorded on the nanoparticles suspension in isopropanol using a Jasco V-770 spectrophotometer. SEM images were acquired using a TESCAN SEM with an acceleration voltage of 5 kV. Transmission electron microscopy was performed using a nonaberration-corrected transmission electron microscope (TALOS F200X, Thermo Scientific, Eindhoven, The Netherlands) operating at 200 kV. The sample images were captured using a 16Mpxls CMOS camera with an exposure time of 1 s. Samples were observed in TEM with a nonaberration corrected transmission electron microscope (TALOS F200X, ThermoScientific, Eindhoven, Netherland) operated at 200 kV. XRD was performed on a Malvern PANanalytical Empyrean Series-3 diffractometer (Cu Kα radiation, Malvern Panalytical Ltd) at 40 kV and 40 mA. Scanning electron microscope images were taken using TESCAN at an accelerating voltage of 5 kV. X-ray and ultraviolet photoelectron spectroscopy were carried out with a Kratos Axis UltraDLD spectrometer, to evaluate the chemical composition and to estimate the position of the VBM and the work function of the materials under investigation. For XPS measurements, high-resolution spectra of Ag 3d and Bi 4f peaks were acquired at a pass energy of 10 eV, using a monochromatic Al Kα source (15 kV, 20 mA). UPS measurements were performed using a He I (21.22 eV) discharge lamp, on an area of 55 µm in diameter, at a pass energy of 10 eV and with a dwell time of 100 ms. The work function (position of the Fermi level with respect to the vacuum level) was measured from the threshold energy for the emission of secondary electrons during He I excitation. A −9.0 V bias was applied to the sample to precisely determine the low-kinetic-energy (i.e., high-binding-energy) cutoff, as discussed by Helander and colleagues [45]. The Ag K-edge EXAFS measurements were performed at room temperature in transmission mode

26884062, 2026, 5, Downloaded from https://onlinelibrary.wiley.com/doi/10.1002/sstr.70487 by Politecnico Di Torino Sist. Bibl Del Polit Di Torino, Wiley Online Library on [25/05/2026]. See the Terms and Conditions (https://onlinelibrary.wiley.com/terms-and-conditions) on Wiley Online Library for rules of use; OA articles are governed by the applicable Creative Commons License

on the beamline SAMBA at the SOLEIL synchrotron. The Si (2 2 0) monochromator was calibrated to 25 515.6 eV at the first inflection point of the Ag foil XANES spectrum. The sample powder was mixed uniformly with chitosan powder with an optimized ratio. The mixtures were pressed into 5 mm-diameter pellets and sealed in 8 μm-thick kapton. The size of the beam was 1×1 mm^2 and the X-ray energy was scanned around the Ag K edge between 25.3 keV and 26.3 keV with 5 eV step size and 0.08 s counting time per point. Apart from the samples, an Ag metallic foil was also measured as a reference. The analysis of the EXAFS was performed with the Demeter software package [46]. The theoretical backscattering amplitudes and phase shifts for single and multiple scattering of the different structures were obtained using FEFF. Artemis was then used to fit the theoretical values to the experimental data.

4.4 | Preparation of Photoanodes

FTO substrates were cut into rectangular shapes of 1×2 cm and cleaned in an ultrasonic bath using detergent, ethanol, and acetone. Between each cleaning step, the substrates were dried with compressed air. The substrates were masked using Kapton tape to leave an area of 1 cm^2 exposed. A thin gold contact was sputtered (30 mA and 100 s) on the exposed area. Nanoparticles inks were prepared with a concentration of 0.5 mg/mL in isopropanol and sonicated for roughly 30 min prior to deposition. The photoanodes were prepared via USSC of the suspensions, using a Nadetech Innovations Ultrasonic Lab Spray Coater. A N_2 pressure of 0.10 bar, nozzle speed of 400 mm/min, and working flow of the suspension of 25 mL h^{-1} were used. The hotplate was set to 150°C, and the patterns parameters used were five passage steps with a distance of 2 mm between each step. Annealing of the electrodes was performed in a N_2 filled tube furnace at 250°C for 1 h, with a heating ramp of 2.5°C min^{-1}.

4.5 | Deposition of Protection Layers by ALD

The conformal ZnO coating on the photoanodes was achieved by ALD. Thermal ALD was performed using a ForgeNano Theia ALD setup. Dimethyl zinc (DMZ) was used as a metal-organic precursor and water vapor was used as coreagent. The precursors were conveyed through fast pneumatic valves (FPVs) by controlling the time of the valve opening. The vapor-phase precursors were heated up at 140°C flowing through the FPVs and then conveyed inside the reaction chamber where the temperature was set to 150°C. A single growth cycle for ZnO was set up to have a DMZ dose time of 30 ms, with FPVs opened up to let the precursor flow inside the chamber, followed by 100 ms of hold time where a N_2 flow is used at the edge of the chamber to prevent the precursor to be pumped down and allowed to interact with the surface. The purge time was set to 300 ms. The second half cycle was set to have 35 ms dose time for H_2O, 250 ms hold time and a final 300 ms N_2 purge time. The process allowed slow growth of ZnO per each cycle and was repeated for a total of 2400 cycles to achieve conformal coating of the sprayed nanoparticles. By growing ZnO on a flat silicon surface, the thickness of the film was evaluated via spectroscopic ellipsometry yielding (17 ± 2) nm. The effectiveness of the coating process was evaluated by photoelectrochemical stability characterization as shown in Figure 6.

4.6 | Electrochemical Characterization

CV experiments were performed by means of a Metrohm Autolab PGSTAT302N potentiostat in a three-electrode configuration, with 1 M KOH as the electrolyte, $AgBiS_2$ as the working electrode, Hg/HgO as the reference electrode, and a Pt wire as the counter electrode. CVs were performed at a scan rate of 20 mV s^{-1} under dark conditions. Open circuit chronopotentiometry was performed in a 0.5 M ascorbate solution (pH 7.57). Ascorbate was employed as hole scavenger, as the ample driving force for the oxidation process ensures virtually unitary interfacial charge transfer efficiency and significantly suppress charge recombination. The latter phenomenon can play a crucial role in pinning the Fermi level at localized states, leading to a situation in which the measured value of E_{FB} appears more positive than expected. Therefore, the use of ascorbate can mitigate the shift of the measured value of E_{FB} [47]. The photoanode was initially positively polarized in the dark at 0.433V versus RHE (−0.2V vs. HgO) for 150 s, after which it was allowed to reach a stable potential in the dark. Once a steady potential was reached, the substrate was irradiated with AM 1.5G light, which causes the generation of electrons and holes that may either recombine or undergo separation and storage within the semiconductor. The photoelectrode was illuminated until a stable photopotential value was obtained. Restoring the dark conditions after this causes a decay of the photovoltage owing to recombination.

4.7 | Photoelectrochemical Characterization

PEC measurements were performed with an Autolab PGSTAT204 potentiostat, and a Xenon Lamp Spectral Products ASB-XE-E180 light source, set to 100 mW cm^{-2} using an Oriel PV reference cell system. The setup employed a three-electrode configuration using a platinum wire counter electrode, an Ag/AgCl (saturated KCl) reference electrode, and a platinum clip for the working electrode. Potentials recorded against Ag/AgCl were converted to RHE scale using the equation

$$E(\text{V vs. RHE}) = E(\text{V vs. Ag/AgCl}) + 0.197\ \text{V} + 0.059\ \text{V} \times \text{pH}$$

LSV curves were collected at a scan rate of 5 mV s^{-1}. The samples were illuminated from the front through a quartz window on an Ossila glass PEC cell. IPCE was calculated using 10 Thorlabs FKBV10 hard-coated Vis/NIR bandpass filters with wavelengths from 350 to 800 nm (10 nm fwhm) and the Spectral Product ASB-XE-E180 Xenon Lamp. The IPCE at a specific wavelength (λ) was determined using the formula

$$IPCE(\%) = \frac{1240 \times I_{ph}}{\lambda \times J_{ph}} \times 100$$

where I_{ph} is the photocurrent density, λ is the incident wavelength, and J_{ph} is the incident irradiance, measured using an 843-R Newport optical power meter. Electrochemical impedance spectroscopy (EIS) measurements were conducted using a BioLogic SP-150e potentiostat using a frequency range from 100 kHz to 0.1 Hz Z-fit of the EIS data was performed by EC-Lab software using the RCPE circuit model shown in the SI. Mott–Schottky measurements were performed in the dark at 1 kHz. The donor density (N_d) was obtained from the slope

26884062, 2026, 5, Downloaded from https://onlinelibrary.wiley.com/doi/10.1002/sstr.70487 by Politecnico Di Torino Sist. Bibl Del Polit Di Torino, Wiley Online Library on [25/05/2026]. See the Terms and Conditions (https://onlinelibrary.wiley.com/terms-and-conditions) on Wiley Online Library for rules of use; OA articles are governed by the applicable Creative Commons License

$d(1/C_{SC}^2)/dV$, and the flat band potential can be obtained from the intercept of the linear fit with the X axis ($1/C_{SC}^2 = 0$), both using the formula:

$$N_d = \left(\frac{2}{A^2 e \varepsilon \varepsilon_0}\right)\left(\frac{1}{\frac{d\frac{1}{C_{SC}^2}}{dV}}\right)$$

where A is the electrode area, e is the electron charge, ε is the dielectric constant for $AgBiS_2$ [48] and ϵ_0 is the permittivity in vacuum.

IMPS was carried out with Ivium CompactStat potentiostat coupled with a LED Modulelight. The measurements were performed at 0.9 V versus RHE in 0.5 M sodium ascorbate with a white led ($p = 40\ mW\ cm^{-2}$ at the sample position) with an oscillation amplitude of 10% in a frequency range between 3 kHz to 0.1 Hz. To focus the light spot on the sample, a lens was used; the steady-state intensity of the light was measured with a BP21R photodiode.

Operando XAS were performed at room temperature in reflection mode on the beamline SAMBA at the SOLEIL synchrotron. A self-designed electrochemical cell specifically used for XAS beamline was used for the measurement [49]. Catalysts inks were prepared by ultrasonication of 5 mg of catalysts and 1 mL of ethanol for 20 min. The catalysts were drop casted on the carbon paper electrode for later installation inside the electrochemical cell. The chronoamperometry was performed under applied voltage of 1.23 V vs RHE for 30 min. The XAS spectra were recorded every 3 min.

4.8 | Spectroelectrochemical Characterization

Spectroelectrochemical measurements were carried out with a Jasco V-570 spectrophotometer in a three-electrode configuration, using 20ann-based $AgBiS_2$ as the working electrode, Ag/AgCl as the reference electrode, and a Pt wire as the counterelectrode. The electrode polarization was controlled by a Metrohm Autolab PGSTAT302N potentiostat.

4.9 | Transient Absorption Spectroscopy

Transient absorption measurements were performed in the microsecond time frame. The spectrometer used was comprised of a Continuum Surelite II Nd:YAG laser (1064 nm, FWHM = 6–8 ns, 8 Hz) equipped with a frequency duplicator (532 nm) as excitation and a monochromatized probe light generated by an Applied Photophysics Xenon Lamp combined with an Applied Photophysics monochromator. A selector disk shutter, constructed in-house, was utilized to regulate laser excitation within the 0.1 s time frame. This apparatus, which was controlled by a National Instruments Board, was employed to prevent sample and photomultiplier fatigue. The transmitted light was focused on an Acton SpectraPro 2300i triple grating, dual output spectrograph. For the purpose of conducting fixed-wavelength kinetic studies, a Hamamatsu R3869 photomultiplier was utilized as the detector, with the 50 lines/mm grating being selected for the analysis. The signals generated by the photomultiplier (biased at 470 ± 10 V) were acquired using a TeledyneLeCroy 604Zi oscilloscope (400 MHz, 20 GS/s). For the entirety of the experiments, an oscilloscope input impedance of 350 Ω was utilized. The photoanode, oriented at 45° with respect to both the pump and the probe sources, was placed in a quartz cell containing the electrolytic solution (0.5 M ascorbate solution (pH 7.57) or 1 M KOH). Polarization of the photoanode was achieved with a PGSTAT302N potentiostat (Autolab) in a three-electrode configuration using Ag/AgCl as reference electrode and a Pt wire as the counter electrode. The resulting transient traces were averaged over 150 laser pulses and corrected for the baseline. The laser beam was defocused with a plano-concave lens in order to illuminate the entire active area of the working electrode at the energy of 76±1 mJ/cm^2/pulse. This was achieved by choosing an appropriate combination of attenuating neutral filters, Q-switch (200 μs) and flash lamp (1.40 kV) supply voltage settings.

Acknowledgments

This work was supported by the European Research Council through project JANUS BI (ID: 101041229). Part of this work has been performed at the research infrastructure Piquet (Piemonte Quantum Enabling Technologies), at INRiM, supported by Regione Piemonte. Synchrotron SOLEIL is acknowledged for provision of synchrotron radiation facilities under proposal 20141892. This work is part of the "Technologies for Sustainability" Flagship program of the Istituto Italiano di Tecnologia (IIT). M.M. and S.C. gratefully acknowledge the project "Solar Hydrogen via INtegration of Energy conversion technologies (SHINE)" - ID 37507 - FESR 2021–2027 and S.C. acknowledges financial support from PNRR MUR project ECS_00000033_ECOSISTER.

Open access publishing facilitated by Politecnico di Torino, as part of the Wiley - CRUI-CARE agreement.

Funding

This work was supported by European Research Council (grant no. 101041229).

Conflicts of Interest

The authors declare no conflicts of interest.

Data Availability Statement

The data that support the findings of this study are available from the corresponding author upon reasonable request.

References

1. J. Zheng, H. Zhou, Y. Zou, et al., "Efficiency and Stability of Narrow-Gap Semiconductor-Based Photoelectrodes," *Energy and Environmental Science* 12 (2019): 2345.

2. D. R. Santos, S. Shukla, and B. Vermang, "Prospects of Copper–Bismuth Chalcogenide Absorbers for Photovoltaics and Photoelectrocatalysis," *Journal of Materials Chemistry A* 11 (2023): 22087.

3. A. Gautam, S. Sk, and U. Pal, "Recent Advances in Solution Assisted Synthesis of Transition Metal Chalcogenides for Photo-Electrocatalytic Hydrogen Evolution," *Physical Chemistry Chemical Physics* 24 (2022): 20638.

4. C. Y. Toe, S. Zhou, M. Gunawan, X. Lu, Y. H. Ng, and R. Amal, "Recent Advances and the Design Criteria of Metal Sulfide Photocathodes and Photoanodes for Photoelectrocatalysis," *Journal of Materials Chemistry A* 9 (2021): 20277.

26884062, 2026, 5, Downloaded from https://onlinelibrary.wiley.com/doi/10.1002/sstr.70487 by Politecnico Di Torino Sist. Bibl Del Polit Di Torino, Wiley Online Library on [25/05/2026]. See the Terms and Conditions (https://onlinelibrary.wiley.com/terms-and-conditions) on Wiley Online Library for rules of use; OA articles are governed by the applicable Creative Commons License

5. P. Da, M. Cha, L. Sun, Y. Wu, Z. S. Wang, and G. Zheng, "High-Performance Perovskite Photoanode Enabled by Ni Passivation and Catalysis," *Nano Letters* 15 (2015): 3452.

6. M. T. Hoang, N. D. Pham, J. H. Han, J. M. Gardner, and I. Oh, "Integrated Photoelectrolysis of Water Implemented On Organic Metal Halide Perovskite Photoelectrode," *ACS Applied Materials and Interfaces* 8 (2016): 11904.

7. I. Poli, T. Gatti, Y. Li, et al., "Lead-Free Perovskites and Derivatives for Photogeneration: A Roadmap to Sustainable Approaches for Photovoltaics and Photo(electro)catalysis," *Journal of Physics: Energy* 8 (2026): 011501, https://doi.org/10.1088/2515-7655/ae2540.

8. Y. T. Huang, S. R. Kavanagh, D. O. Scanlon, A. Walsh, and R. L. Z. Hoye, "Perovskite-Inspired Materials for Photovoltaics and beyond—from Design to Devices," *Nanotechnology* 32 (2021): 132004, https://doi.org/10.1088/1361-6528/abcf6d.

9. M. Liu, G. Krishnamurthy Grandhi, B. Al-Anesi, et al., "Water-Resistant Perovskite-Inspired Copper/Silver Pnictohalide Nanocrystals for Photoelectrochemical Water Splitting," *Electrochimica Acta* 462 (2023): 142734, https://doi.org/10.1016/j.electacta.2023.142734.

10. F. Ünlü, M. Deo, S. Mathur, T. Kirchartz, and A. Kulkarni, "Bismuth-Based Halide Perovskite and Perovskite-Inspired Light Absorbing Materials for Photovoltaics," *Journal of Physics D: Applied Physics* 55 (2021): 113002, https://doi.org/10.1088/1361-6463/ac3033.

11. G. K. Grandhi, N. S. M. Viswanath, M. Righetto, et al., "Silver–Bismuth Perovskite-Inspired Materials: Chemistry, Optoelectronic Properties, and Emerging Applications in Photovoltaics and beyond," *Journal of Materials Chemistry A* 14 (2026): 60–89, https://doi.org/10.1039/D5TA06180F.

12. J. Lee, C. Sun, J. Park, et al., "High Efficiency (>10%) $AgBiS_2$ Colloidal Nanocrystal Solar Cells with Diketopyrrolopyrrole-Based Polymer Hole Transport Layer," *Advanced Materials* 37 (2025): 2413081, https://doi.org/10.1002/adma.202413081.

13. X. Li, H. Yu, X. Ma, et al., "Thin Film $AgBiS_2$ Solar Cells with over 10% Power Conversion Efficiency Enabled by Vapor-Assisted Solution Process Treatment," *Chemical Engineering Journal* 495 (2024): 153328, https://doi.org/10.1016/j.cej.2024.153328.

14. Q. Zhong, B. Zhao, Y. Ji, et al., "Solvent-Engineering-Assisted Ligand Exchange Strategy for High-Efficiency $AgBiS_2$ Quantum Dot Solar Cells," *Angewandte Chemie International Edition* 63 (2024): e202412590, https://doi.org/10.1002/anie.202412590.

15. H. J. Kim, J. Y. Park, Y. J. Choi, et al., "Homogeneously Blended Donor and Acceptor $AgBiS_2$ Nanocrystal Inks Enable High-Performance Eco-Friendly Solar Cells with Enhanced Carrier Diffusion Length," *Advanced Energy Materials* 15 (2025): 2404552, https://doi.org/10.1002/aenm.202404552.

16. Y. Ji, Q. Zhong, X. Yang, et al., "Surface Engineering Enables Efficient $AgBiS_2$ Quantum Dot Solar Cells," *Nano Letters* 24 (2024): 10418.

17. J. T. Oh, S. Y. Bae, S. R. Ha, et al., "Water-Resistant $AgBiS_2$ Colloidal Nanocrystal Solids for Eco-Friendly Thin Film Photovoltaics," *Nanoscale* 11 (2019): 9633.

18. J. Y. Park, G. Park, S. Y. Bae, et al., "Ecofriendly $AgBiS_2$ Nanocrystal Photoanode for Highly Efficient Visible-Light-Driven Photoelectrochemical Water Splitting," *ACS Applied Energy Materials* 6 (2023): 3872.

19. F. Viñes, G. Konstantatos, and F. Illas, "Bandgap Engineering by Cationic Disorder: Case Study on $AgBiS_2$," *Physical Chemistry Chemical Physics* 19 (2017): 27940.

20. N. Ha, G. H. Lee, J. Park, et al., "Dithiocarbamate-Based Solution Processing for Cation Disorder Engineering in $AgBiS_2$ Solar Absorber Thin Films," *Advanced Energy Materials* 15 (2025): 2402099, https://doi.org/10.1002/aenm.202402099.

21. Y. T. Huang and R. L. Z. Hoye, "Tuning the Optoelectronic Properties of Emerging Solar Absorbers through Cation Disorder Engineering," *Nanoscale* 16 (2024): 10155.

22. M. Righetto, Y. Wang, K. A. Elmestekawy, et al., "Cation-Disorder Engineering Promotes Efficient Charge-Carrier Transport in $AgBiS_2$ Nanocrystal Films," *Advanced Materials* 35 (2023): 2305009, https://doi.org/10.1002/adma.202305009.

23. Y. Wang, S. R. Kavanagh, I. Burgués-Ceballos, A. Walsh, D. Scanlon, and G. Konstantatos, "Cation Disorder Engineering Yields $AgBiS_2$ Nanocrystals with Enhanced Optical Absorption for Efficient Ultrathin Solar Cells," *Nature Photonics* 16 (2022): 235.

24. J. K. Kesavan, F. D'acapito, P. Scardi, et al., "Cation Disorder and Local Structural Distortions in $Ag_xBi_{1-x}S_2$ Nanoparticles," *Nanomaterials* 10 (2020): 316, https://doi.org/10.3390/nano10020316.

25. L. Hu, R. J. Patterson, Z. Zhang, et al., "Enhanced Optoelectronic Performance in $AgBiS_2$ Nanocrystals Obtained *via* an Improved Amine-Based Synthesis Route," *Journal of Materials Chemistry C* 6 (2018): 731.

26. J. Chen, Q. Zhong, E. Sirotti, et al., "Ligand-Tuned $AgBiS_2$ Planar Heterojunctions Enable Efficient Ultrathin Solar Cells," *ACS Nano* 18 (2024): 33348.

27. D. Chen, S. B. Shivarudraiah, P. Geng, et al., "Solution-Processed, Inverted $AgBiS_2$ Nanocrystal Solar Cells," *ACS Applied Materials and Interfaces* 14 (2022): 1634.

28. E. Gu, X. Lin, X. Tang, et al., "Single Molecular Precursor Ink for $AgBiS_2$ Thin Films: Synthesis and Characterization," *Journal of Materials Chemistry C* 6 (2018): 7642.

29. J. van Embden and E. Della Gaspera, "Ultrathin Solar Absorber Layers of Silver Bismuth Sulfide from Molecular Precursors," *ACS Applied Materials and Interfaces* 11 (2019): 16674.

30. L. Jiang, Y. Li, J. Peng, et al., "Solution-Processed $AgBiS_2$ Photodetectors from Molecular Precursors," *Journal of Materials Chemistry C* 8 (2020): 2436.

31. N. Pai, J. Lu, D. C. Senevirathna, et al., "Spray Deposition of $AgBiS_2$ and Cu_3BiS_3 Thin Films for Photovoltaic Applications," *Journal of Materials Chemistry C* 6 (2018): 2483.

32. S. Ma, S. Sansoni, T. Gatti, P. Fino, G. Liu, and F. Lamberti, "Research Progress on Homogeneous Fabrication of Large-Area Perovskite Films by Spray Coating," *Crystals* 13 (2023): 216, https://doi.org/10.3390/cryst13020216.

33. A. E. X. Gavim, M. R. P. da Cunha, E. R. Spada, et al., "Water-Suspended MoO_3 Nanoparticles Prepared by LASIS and Fast Processing as Thin Film by Ultrasonic Spray Deposition," *Solar Energy Materials and Solar Cells*, 200 (2019): 109986, https://doi.org/10.1016/j.solmat.2019.109986.

34. J. Stryckers, L. D'Olieslaeger, J. V. M. Silvano, et al., "Layer Formation and Morphology of Ultrasonic Spray Coated Polystyrene Nanoparticle Layers," *Physica Status Solidi (A) Applications and Materials Science* 213 (2016): 1441.

35. M. De Dai, Q. Zhang, H. Dong, and Y. W. Zhang, "Enhanced Light Driven CO_2 Conversion Based on Silver Bismuth Sulfide Hollow Octahedrons Coated with Amorphous Metal–Organic Frameworks," *Materials Advances* 5 (2023): 1715.

36. M. G. Ju, J. Dai, L. Ma, Y. Zhou, and X. C. Zeng, "$AgBiS_2$ as a Low-Cost and Eco-Friendly All-Inorganic Photovoltaic Material: Nanoscale Morphology–Property Relationship," *Nanoscale Advances* 2 (2020): 770.

37. R. Harris-Lee, F. Marken, C. L. Bentley, J. Zhang, and A. L. Johnson, "A Chemist's Guide to Photoelectrode Development for Water Splitting – the Importance of Molecular Precursor Design," *EES Catalysis* 1 (2023): 832.

38. D. S. Ellis, A. Tsyganok, P. Ghigna, et al., "Operando X-Ray Absorption Spectroscopy (XAS) Observation of Photoinduced

26884062, 2026, 5, Downloaded from https://onlinelibrary.wiley.com/doi/10.1002/sstr.70487 by Politecnico Di Torino Sist. Bibl Del Polit Di Torino, Wiley Online Library on [25/05/2026]. See the Terms and Conditions (https://onlinelibrary.wiley.com/terms-and-conditions) on Wiley Online Library for rules of use; OA articles are governed by the applicable Creative Commons License

Oxidation in FeNi (Oxy)hydroxide Overlayers on Hematite (α-Fe_2O_3) Photoanodes for Solar Water Splitting," *Langmuir* 36 (2020): 11564.

39. J. Timoshenko and B. Roldan Cuenya, "*In Situ*/ *Operando* Electrocatalyst Characterization by X-Ray Absorption Spectroscopy," *Chemical Reviews* 121 (2021): 882.

40. R. Kumar, B. Rakheja, N. Lamminen, et al., "Mechanistic Insights into Ionic Conduction in Lead Halide Perovskites and Perovskite-Inspired Materials," *Advanced Energy Materials*. (2025), https://doi.org/10.1002/aenm.202503331.

41. Y. T. Huang, D. Nodari, F. Furlan, et al., "Fast Near-Infrared Photodetectors Based on Nontoxic and Solution-Processable $AgBiS_2$," *Small* 20 (2024): 2310199, https://doi.org/10.1002/smll.202310199.

42. C. G. Bellido, M. Mazzanti, K. Ranu, et al., "Hybrid Molecular Photoanodes for Water Oxidation Based on Electropolymerized Cu Macrocyclic Complexes on $BiVO_4$-WO_3," *Advanced Energy Materials* 15 (2025): e00253, https://doi.org/10.1002/aenm.202500253.

43. R. Altieri, F. Schmitz, M. Schenker, et al., "Development of an Automated SILAR Method for the Sustainable Fabrication of BiOI/TiO_2 Photoanodes," *Energy Advances* 3 (2024): 2564.

44. A. Kargar, K. Sun, Y. Jing, et al., "Tailoring n-ZnO/p-Si Branched Nanowire Heterostructures for Selective Photoelectrochemical Water Oxidation or Reduction," *Nano Letters* 13 (2013): 3017.

45. M. G. Helander, M. T. Greiner, Z. B. Wang, and Z. H. Lu, "Pitfalls in Measuring Work Function Using Photoelectron Spectroscopy," *Applied Surface Science* 256 (2010): 2602.

46. B. Ravel and M. Newville, "ATHENA, ARTEMIS, HEPHAESTUS: Data Analysis for X-Ray Absorption Spectroscopy Using IFEFFIT," *Synchrotron Radiat* 12 (2005): 537–541.

47. E. Koshevoy, E. Gribov, D. Polskikh, et al., "Photoelectrochemical Methods for the Determination of the Flat-Band Potential in Semiconducting Photocatalysts: A Comparison Study," *Langmuir* 39 (2023): 13466.

48. B. Bellal, M. H. Berger, and M. Trari, "Physical and Photoelectrochemical Properties of Spherical Nanoparticles of α-$AgBiS_2$," *Journal of Solid State Chemistry* 254 (2017): 178.

49. A. Zitolo, N. Ranjbar-Sahraie, T. Mineva, et al., "Identification of Catalytic Sites in Cobalt-Nitrogen-Carbon Materials for the Oxygen Reduction Reaction," *Nature Communications* 8 (2017): 957, https://doi.org/10.1038/s41467-017-01100-7.

Supporting Information

Additional supporting information can be found online in the Supporting Information section.

26884062, 2026, 5, Downloaded from https://onlinelibrary.wiley.com/doi/10.1002/sstr.70487 by Politecnico Di Torino Sist. Bibl Del Polit Di Torino, Wiley Online Library on [25/05/2026]. See the Terms and Conditions (https://onlinelibrary.wiley.com/terms-and-conditions) on Wiley Online Library for rules of use; OA articles are governed by the applicable Creative Commons License